



Enhanced oxygen reduction reaction for Zn-air battery at defective carbon fibers derived from seaweed polysaccharide

Xiaoliang Zhao^a, Xuezheng Yu^a, Shishan Xin^a, Shuai Chen^b, Chaosheng Bao^a, Wenqing Xu^a, Jingfei Xue^a, Bin Hui^a, Jianwei Zhang^{a,*}, Xilin She^{a,*}, Dongjiang Yang^a

^a School of Environmental Science and Engineering, State Key Laboratory of Bio-fibers and Eco-textiles, Shandong Collaborative Innovation Center of Marine Bio-based Fibers and Ecological Textiles, Qingdao University, Qingdao 266071, PR China

^b State Key Laboratory of Coal Conversion, Institute of Coal Chemistry, Chinese Academy of Science, Taiyuan 030001, PR China

ARTICLE INFO

Keywords:

Seaweed polysaccharide
Defective carbon fiber
Oxygen reduction reaction
Zinc-air batteries

ABSTRACT

Carbon fibers with intrinsic carbon defects (D-CFs) were fabricated through heteroatoms doping and de-doping using seaweed polysaccharide as the precursor. When evaluated as oxygen reduction reaction (ORR) electrocatalyst, D-CFs display an initial potential of 0.92 V (vs. RHE) and a limiting diffusion current density of 5.38 mA·cm⁻² in KOH electrolyte (0.1 M). The high peak power density of zinc-air batteries (ZABs) assembled by D-CFs is 238 mW·cm⁻², that is much better than commercial Pt/C (154 mW·cm⁻²). In the light of density functional theory (DFT) results, enriched electrons in defects make the hybridization energy levels of active defective sites and adsorbed oxygen atoms rise to Fermi level, indicating that O₂ molecules are inclined to be adsorbed onto defective carbon atoms. Therefore, abundant renewable seaweed sources, together with the excellent ORR catalytic activity, make D-CFs as the substitute of Pt/C catalyst for large-scale application of ZABs.

1. Introduction

As next-generation energy storage and conversion technique, zinc-air batteries (ZABs) have drawn widespread concern due to the merits of environmental friendliness and high theoretical energy density [1,2]. However, the adverse kinetics of oxygen reduction reaction (ORR) at the cathode leads to the unsatisfactory performance of ZABs [3]. Although platinum (Pt)-based catalysts can promote the ORR kinetics, their scarce reserve, high cost, and general stability limit their broad application [4–6]. Thus, developing economic electrocatalysts with excellent ORR performance is necessary.

Recently, various ORR catalysts as alternatives of Pt have been researching, containing carbon materials [7,8], transition metal nitrides [9,10], ternary thiospinel [11], carbon nitride [12,13], transition metal chalcogenides [14,15], and conjugated polymers [16,17]. Due to abundant structural variety, good conductivity, and low cost, carbon-based nanomaterials have aroused widespread concern in recent years. For original carbon-based materials, the excellent conductivity is beneficial to the electron transfer during ORR process, but the complete sp² conjugated carbon atoms structure can not provide the active sites for O₂ adsorption and reaction, which leads to their poor ORR activity

[18,19]. Correspondingly, heteroatoms doping can effectively boost the activity of original carbon catalysts [20,21]. Because the doped heteroatoms generally exhibit the higher electronegativity than carbon atoms, inducing a partial positive charge around carbon atoms which is in favor of ORR [22,23]. However, owing to the limitation of electronic environment changes, ORR performances of heteroatoms-doped carbon nanomaterials are usually incomparable to those of Pt-based catalysts [24].

In recent years, defect engineering has played a significant effect on the change of surface properties and the optimization of electronic structures for nanomaterials [25–27]. For instance, Jia et al. reported a two-dimensional graphene material with intrinsic carbon defects which are obtained by removing doped nitrogen atoms. Although both N-doping and defect engineering make graphene reveal enhanced ORR catalytic activity than original graphene, the initial potential and limiting diffusion current density of the defective graphene are more positive and larger than those of N-doped graphene [28]. It is attributed to that defects can further destroy the complete structure of sp² conjugated carbon atoms and then make carbon atoms at the edge of defects obtain the favorable HOMO/LUMO orbital distributions [28]. It accelerates the O₂ molecules adsorption and reaction at defective carbon

* Corresponding authors.

E-mail addresses: sdqdzjw@qdu.edu.cn (J. Zhang), xlshe@qdu.edu.cn (X. She).

<https://doi.org/10.1016/j.apcatb.2021.120785>

Received 30 June 2021; Received in revised form 29 September 2021; Accepted 30 September 2021

Available online 3 October 2021

0926-3373/© 2021 Elsevier B.V. All rights reserved.

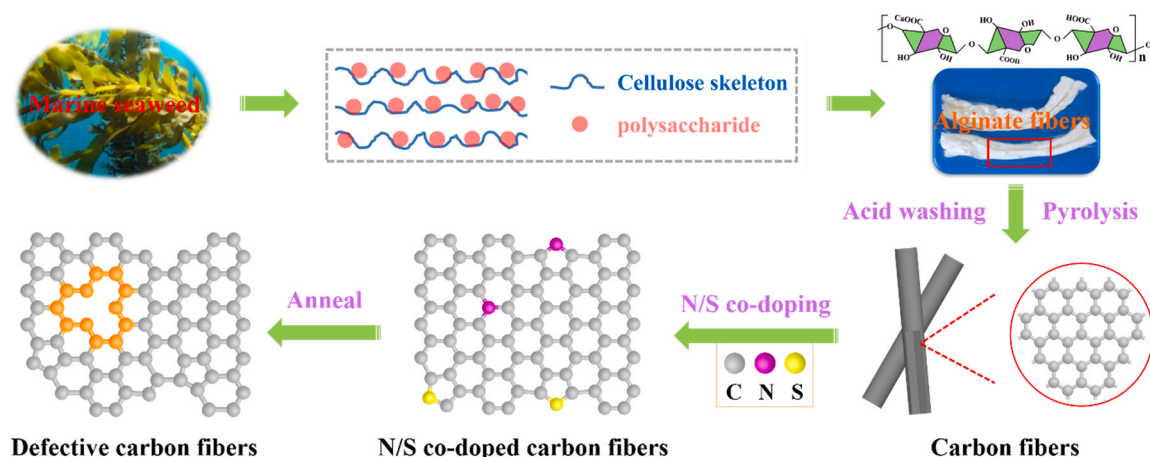


Fig. 1. The synthesis process of CFs, N/S-CFs and D-CFs.

atoms, resulting in excellent ORR catalytic performance [29,30]. However, the preparation of defective ORR catalysts usually focuses on single-layered graphene or single-walled carbon nanotubes, so their synthesis cost is not lower than that of Pt/C. Apparently, the high cost of ORR catalysts has become the stumbling block to realize the application of ZABs [31,32].

In this work, carbon fibers with intrinsic carbon defects (D-CFs) as pure carbon material were fabricated by the removal of previously doped N/S atoms in N/S co-doped CFs, which were prepared by using renewable calcium alginate fibers as precursor. The D-CFs reveal prominent catalytic activity toward ORR, since one-dimensional fibers exhibit excellent electron transport, superior stability, and high surface area. For instance, the D-CFs reaches an initial potential of 0.92 V vs. RHE and limiting diffusion current of $5.38 \text{ mA}\cdot\text{cm}^{-2}$ under 0.1 M KOH solution, which are comparable with those of Pt/C and better than those of N/S co-doped carbon fibers (N/S-CFs) (the initial potential: 0.85 V vs. RHE; limiting diffusion current: $3.56 \text{ mA}\cdot\text{cm}^{-2}$). Moreover, the ZAB employing D-CFs catalyst achieves higher peak power density of $238 \text{ mW}\cdot\text{cm}^{-2}$ than that of Pt/C catalyst ($154 \text{ mW}\cdot\text{cm}^{-2}$). The density functional theory (DFT) results demonstrate that defectives carbon generated from the N/S removal could reduce the energy of 2p orbitals of adsorbed O atoms via the electronic reflux, approaching the hybridization energy levels of defective C atom and adsorbed O atom closely to Fermi level. This means O_2 molecules are more inclined to adsorb on defective carbon atoms than that of CFs and N/S-CFs, boosting the ORR performance of D-CFs. This work supplies a promising strategy to

fabricate metal-free ORR catalysts from marine biomass with outstanding activity for electrochemical storage devices.

2. Experimental section

2.1. Materials

2.1.1. Preparation of carbon fibers (CFs)

Firstly, prepared calcium alginate fibers (8.37 g) were kept at 900°C for 2 h under Ar atmosphere [33]. Secondly, the obtained fibers were soaked in the HCl solution (1.0 M). Finally, pure water was used to repeatedly wash the product until the pH of washing solution was ~ 7 . And then the produce was dried at 60°C for 30 min after the suction filtration, obtaining CFs (1.53 g).

2.1.2. Preparation of N/S co-doped carbon fibers (N/S-CFs)

Thioacetamide (15.30 g) placed in front of the gas flow direction and the CFs (1.53 g) placed behind the gas flow direction, then were heated at 600°C for 1 h under Ar atmosphere.

2.1.3. Preparation of defective carbon fibers (D-CFs)

The N/S-CFs were heated at 1000°C for 60 min in argon.

2.2. Methods

Details about materials preparation, structural representations,

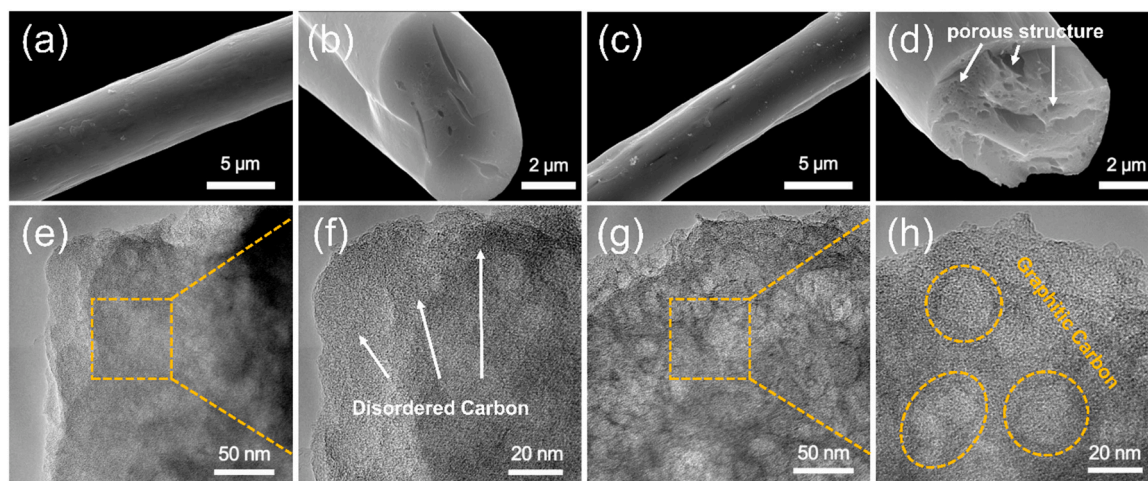


Fig. 2. SEM images of (a, b) N/S-CFs and (c, d) D-CFs. Low- and high-resolution TEM images of (e, f) N/S-CFs and (g, h) D-CFs.

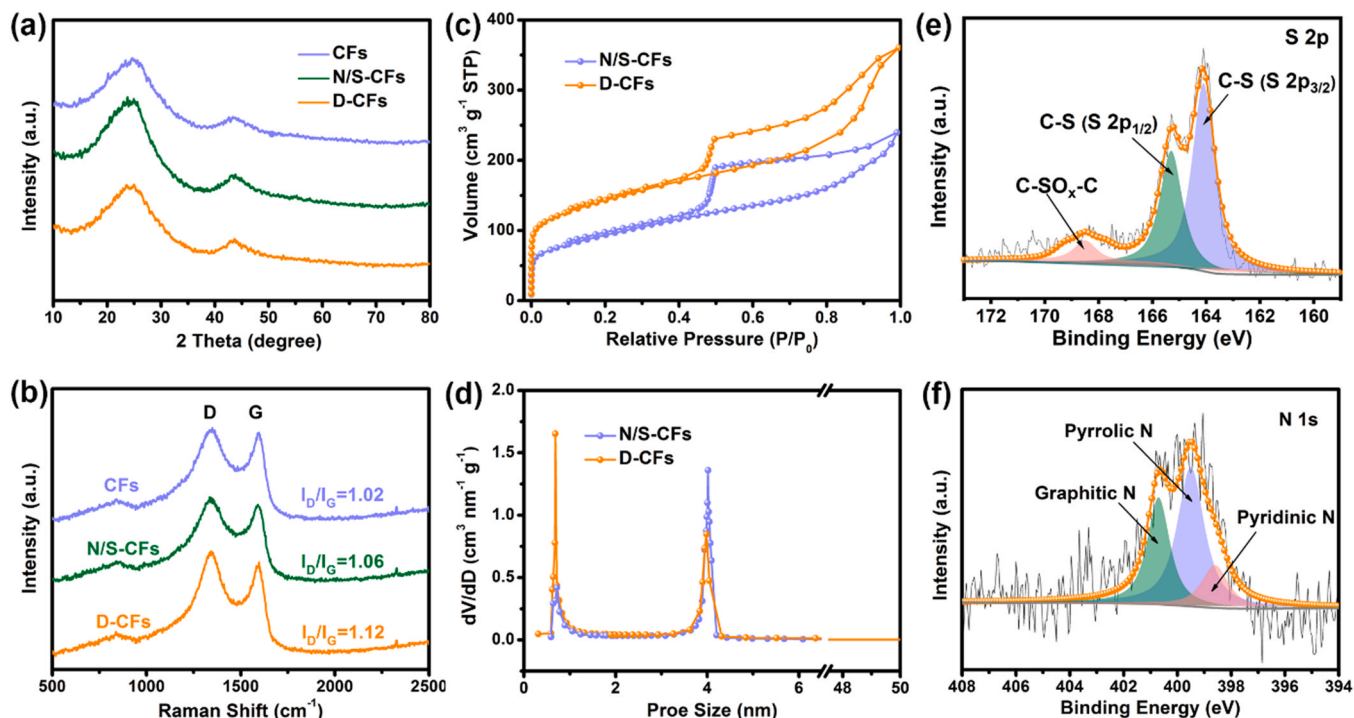


Fig. 3. (a) XRD patterns and (b) Raman spectra of CFs, N/S-CFs, and D-CFs. (c) Nitrogen adsorption/desorption isotherms and (d) corresponding calculated pore size distribution of N/S-CFs and D-CFs. High-resolution XPS spectra of (e) S 2p and (f) N 1s of N/S-CFs.

performance tests, and DFT calculations are supplied in [Supporting Information](#).

3. Results and discussion

3.1. Preparation and characterization of CFs, N/S-CFs, and D-CFs catalysts

Molecular structures of sodium alginate and the manufacturing process of calcium alginate fibers (CAFs) are shown in [Fig. S1](#). The Na^+ ions in sodium alginate molecules were replaced by Ca^{2+} ions through the ion exchange. And then insoluble calcium alginate was converted into white CAFs via the wet spinning. The manufacturing procedure of carbon fibers with intrinsic carbon defects (D-CFs) is displayed in [Fig. 1](#). Firstly, Ca^{2+} ions were converted into CaO particles after carbonization of CAFs, which were removed by acid washing, thus obtaining carbon fibers (CFs) [34]. Subsequently, N and S atoms from the thioacetamide were doped into CFs by the pyrolysis, which partially replace carbons atoms of CFs and then generate N/S co-doped CFs (N/S-CFs). Finally, doped N and S heteroatoms in N/S-CFs were removed via annealing, forming D-CFs in which defect sites were generated through the recombination of carbon atoms. Electronic structure change of defective carbon atoms can enhance ORR catalytic activity [35–37].

As shown in [Fig. 2](#), the morphologies of N/S-CFs and D-CFs were observed by scanning electron microscope (SEM) and transmission electron microscopy (TEM). After the N/S-doping and high-temperature de-doping processes, N/S-CFs and D-CFs still retain the one-dimensional fiber morphology with a diameter of $\sim 4 \mu\text{m}$ ([Figs. 2a–d](#) and [S2](#)). From the cross section of fibers, with the removal of doped N and S atoms during the high-temperature annealing processes, more micro- and meso-pores of D-CFs can be observed than those of N/S-CFs ([Fig. 2b](#) and [d](#)). The highly porous structure can expose more accessible active sites and facilitate reactant transport [18]. The TEM images show that N/S-CFs ([Fig. 2e–f](#)) and D-CFs ([Fig. 2g–h](#)) are composed of disordered carbon and graphitic carbon. As shown in [Fig. 2e–h](#), D-CFs expose more defective graphite carbon sites than N-CFs. Graphite carbon generated

from doped-heteroatoms and the formation of defects is distributed around the edge of the pore structure while the disordered carbon is located away from the pore structure [38]. In such graphitic-disordered hybrid structure, graphite carbon endows excellent electrical conductivity and stability, and the disordered carbon offers plenty of active sites from the high surface area.

X-ray diffraction (XRD) patterns of different CFs are shown in [Fig. 3a](#). The CFs, N/S-CFs, and D-CFs all display broad peaks at 24.4° and 43.6° , assigning to (0 0 2) and (1 0 0) facets of graphitic carbon, respectively [39,40]. It demonstrates the macroscopically pure carbon structure of carbon fibers. As displayed in [Fig. 3b](#), Raman spectra of CFs, N/S-CFs, and D-CFs all show the characteristic peaks of D band (1340 cm^{-1}) and G band (1590 cm^{-1}) of carbon materials. Particularly, D and G band represent lattice defects and complete sp^2 hybridization of carbon atoms, respectively. The ratios I_D/I_G of CFs, N/S-CFs, and D-CFs are 1.02, 1.06, and 1.12, respectively. Apparently, doped nitrogen and sulfur atoms can destroy the complete carbon atom lattice. Thus, compared with CFs (1.02), I_D/I_G of N/S-CFs (1.06) is enhanced. In addition, removing the doped heteroatoms can form defects and the conjugated sp^2 hybridized carbon atoms structure is further destroyed. Thus, the I_D/I_G of D-CFs is further enhanced to 1.12 [41]. It indicates the generation of more defect sites in D-CFs, which are beneficial to boost the ORR performance. The N_2 adsorption-desorption isotherm and pore size distribution are exhibited in [Fig. 3c–d](#). Brunauer-Emmett-Teller (BET) surface area of N/S-CFs is $329.0 \text{ m}^2 \cdot \text{g}^{-1}$ while that of D-CFs is $485.2 \text{ m}^2 \cdot \text{g}^{-1}$. Via the IV-type curves, N/S-CFs and D-CFs all have micropores and mesopores ([Fig. 3c](#)). The sharp rise of the curves at low relative pressure (P/P_0 is less than 0.05) indicates the existence of micropores, while the slow rise and hysteresis loops between the relative pressure of 0.45 and 1 indicate the existence of mesopores [42,43]. Pore size distributions of N/S-CFs and D-CFs are further performed in [Fig. 3d](#) and BET results are shown in [Table S1](#). For N/S-CFs and D-CFs, the pore sizes of the micropore and mesopore are $\sim 0.8 \text{ nm}$ and 4.0 nm , respectively. D-CFs reveals more micropores than N/S-CFs due to the escape of gas and volatile in D-CFs during the further de-doping process at higher temperature. Specifically, a large number of micropores in

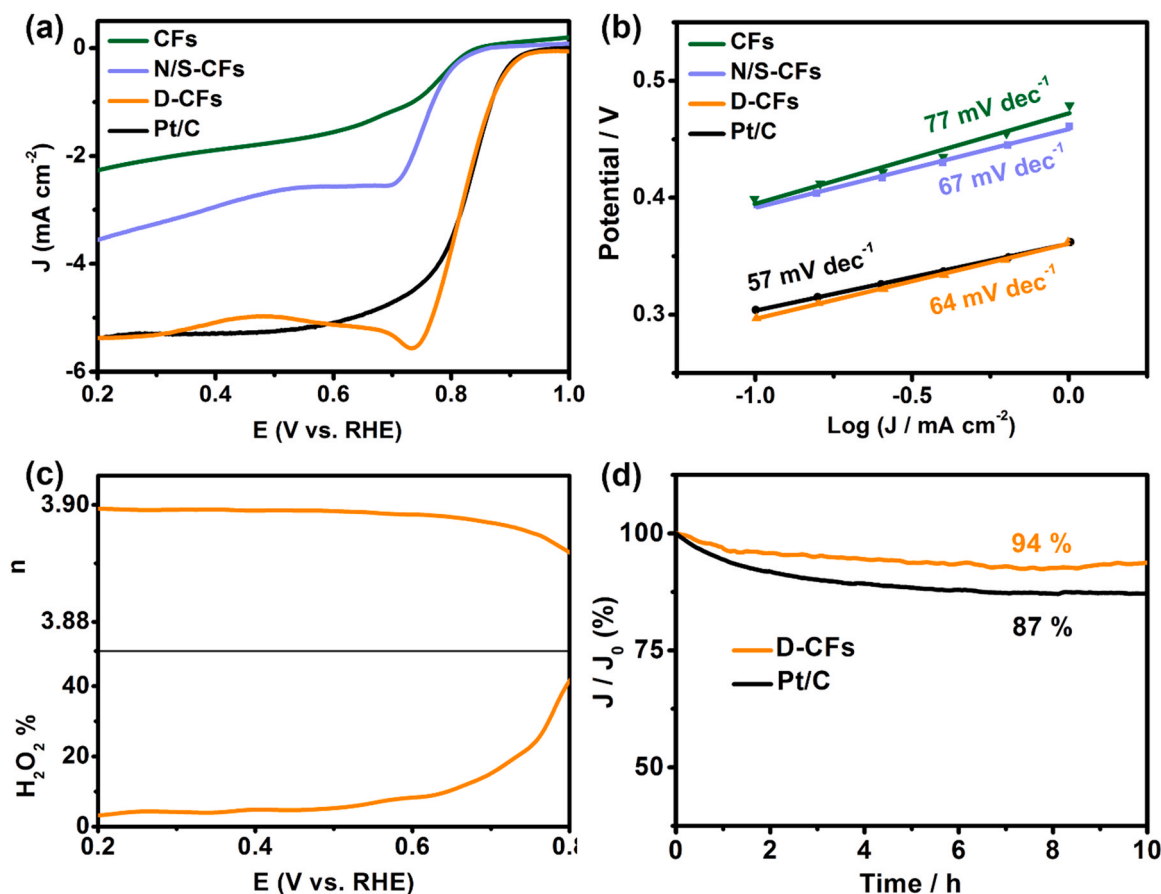


Fig. 4. LSV curves (a) and Tafel plots (b) of CFs, N/S-CFs, D-CFs, and commercial Pt/C. (c) Percentage of HO_2^- and the n of D-CFs. (d) Chronoamperometric response of D-CFs and commercial Pt/C.

D-CFs are beneficial to the adsorption of O_2 molecules, thus enhancing its catalytic performance [44].

To define chemical environments of atoms, X-ray photoelectron spectroscopy (XPS) survey spectra of N/S-CFs and D-CFs are presented in Fig. S3 and S4. The C 1s spectrum of N/S-CFs is divided into four functions at 284.7 eV (C sp^2), 285.1 eV (C-S), 286.0 eV (C-N), and 286.5 eV (C-O) [45,46]. The existences of C-N and C-S prove that N and S atoms are successfully doped in CFs. Furthermore, the high-resolution S 2p and N 1s spectra of N/S-CFs are shown in Fig. 3e and f, respectively. In S 2p spectrum of N/S-CFs, three peaks of the C-S ($\text{S } 2p_{3/2}$), C-S ($\text{S } 2p_{1/2}$), and S ($\text{C-SO}_x\text{-C}$) are observed at 164.1 eV, 165.3 eV, and 168.3 eV, respectively [47]. In addition, N 1s spectrum of N/S-CFs can be fitted to three functions at 398.6 eV, 399.5 eV, and 400.7 eV, corresponding to pyridinic N, pyrrolic N, and graphitic N, respectively [48]. The atomic contents of N/S-CFs and D-CFs based on XPS surveys are shown in Table S2. After annealing at 1000 °C, the contents of nitrogen atoms decreased from 2.01% of N/S-CFs to 1.03% of D-CFs, while the content of sulfur atoms decreased from 1.01% to 0.49% (Figs. S5-S7). After removing the doped heteroatoms in the precursor, the carbon atoms will recombine to form defect sites, thus D-CFs are successfully prepared [28].

3.2. Electrochemical performances

To assess ORR performance of N/S-CFs and D-CFs, linear sweep voltammetry (LSV) measurements on the rotating disk electrode (RDE) were conducted in 0.1 M KOH. As displayed in Fig. 4a, D-CFs exhibit an initial potential (0.92 V vs. RHE) and a limiting diffusion current density ($5.38 \text{ mA}\cdot\text{cm}^{-2}$), that are better than performances of N/S-CFs (0.85 V vs. RHE of initial potential and $3.56 \text{ mA}\cdot\text{cm}^{-2}$ of limiting diffusion

current density) and CFs (0.84 V vs. RHE of initial potential and $2.26 \text{ mA}\cdot\text{cm}^{-2}$ of limiting diffusion current density). In addition, D-CFs exhibit a half-wave potential of 0.84 V vs. RHE, which is equivalent to that of the commercial Pt/C. The corresponding Tafel slopes in Fig. 4b indicate the superior reaction kinetics of D-CFs ($64 \text{ mV}\cdot\text{dec}^{-1}$) than CFs ($77 \text{ mV}\cdot\text{dec}^{-1}$) and N/S-CFs ($67 \text{ mV}\cdot\text{dec}^{-1}$). Electron transfer numbers (n) and peroxide species (HO_2^-) yield of D-CFs in ORR process were determined by the rotating ring disk electrode (RRDE). As revealed in Fig. 4c, D-CFs exhibit that the HO_2^- yield is less than 10% at the voltage between 0.2 V and 0.4 V vs. RHE (based on Eq. (S2)) and a reaction process is close to 4 electron transfer (based on Eq. (S3)). In addition, polarization curves in Fig. S8 are used to study the reaction kinetics of D-CFs during the ORR. Because the diffusion distance becomes short, the current density enhances when the rotating speed increases [49]. On the basis of polarization curves under different potentials, the Koutecky-Levich curves are obtained (based on Eqs. (S4) and (S5)). The linearity and parallelism of the Koutecky-Levich plots (Fig. S9) indicate the first-order reaction kinetics toward the concentration of dissolved oxygen. In addition, electron transfer numbers of D-CFs at 0.25, 0.35 and 0.45 V vs. RHE are calculated to be 4.05, 3.97 and 3.82, respectively, which is consistent with the test results of RRDE. These confirm the reaction process of 4 electron transfer of D-CFs.

Considering the practicability of cathode catalysts, the durability and methanol tolerance need to be assessed. Current-time chronoamperometric responses were recorded for D-CFs and commercial Pt/C. The current density of D-CFs only decreases slightly while 3 M methanol solution was injected into 0.1 M KOH electrolyte at 500 s, but recovers to the original level quickly. However, the methanol oxidation reaction makes that the current density of commercial Pt/C greatly decrease and can't restore to original level (Fig. S10). As displayed in Fig. 4d, after

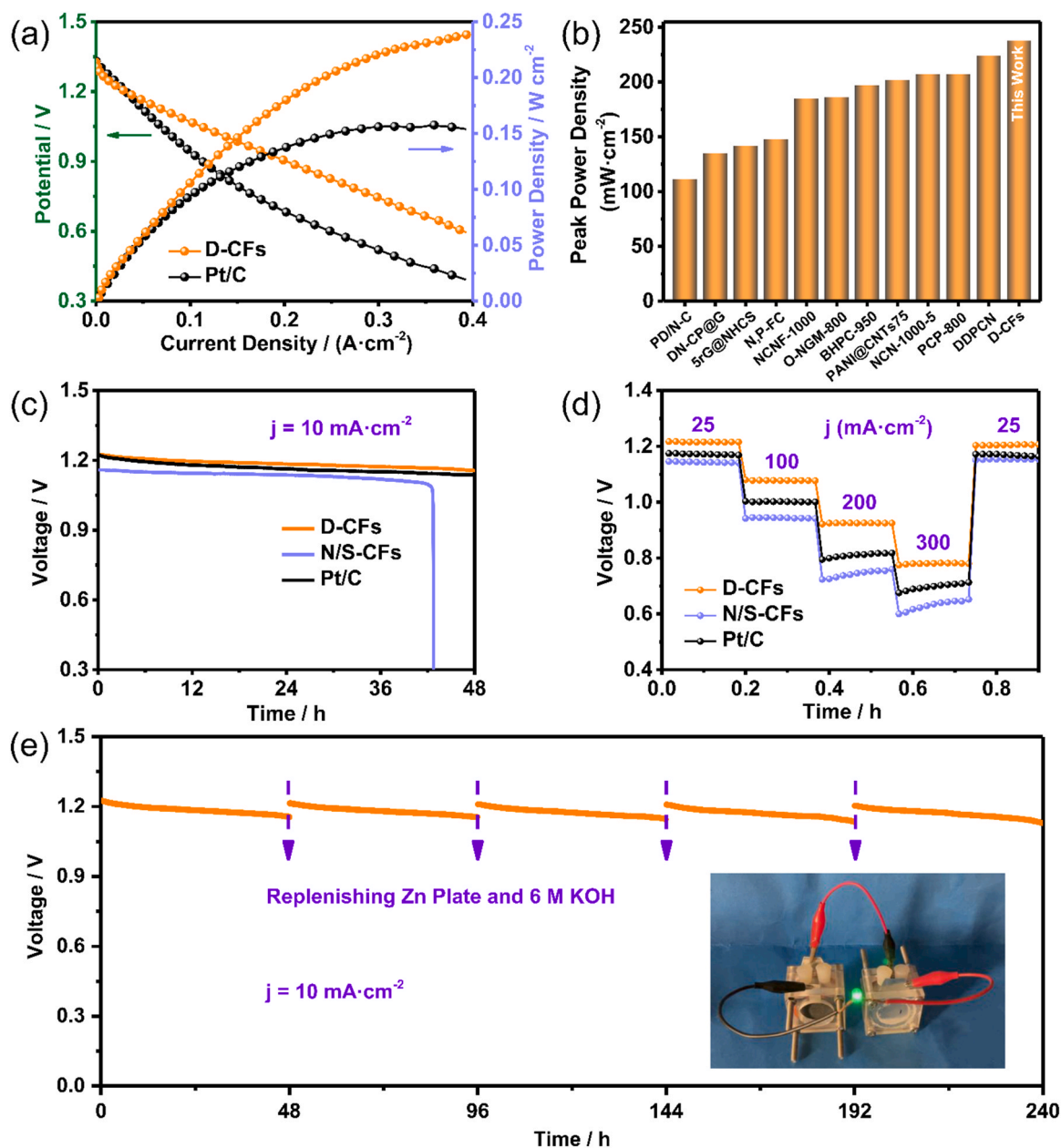


Fig. 5. (a) Polarization and power density curves of the ZABs assembled with D-CFs and Pt/C. (b) Comparison of peak power density between reported metal-free carbon materials and D-CFs. (c) Galvanostatic discharge curves of D-CFs-, N/S-CFs-, and Pt/C-based ZABs at a limiting diffusion current density of 10 mA cm^{-2} . (d) Discharge curves of D-CFs, N/S-CFs, and Pt/C at various discharge current densities. (e) Mechanically recharged D-CFs-based ZABs at 10 mA cm^{-2} (inset: photograph of an LED panel powered by two ZABs in series).

10 h of catalytic reaction, D-CFs maintain a limiting diffusion current density of 94%, while the limiting diffusion current density of Pt/C is only 87%. Owing to the excellent activity and favorable stability, D-CFs are expected to substitute for Pt-based catalysts. To research the component and structure of D-CFs after chronoamperometric test, we have investigated their XRD and SEM data. As shown in Fig. S11, carbon composition of D-CFs do not change, but the fiber structure was crushed.

3.3. Zinc-air battery measurements

To assess the potential of D-CFs for zinc-air battery (ZAB) application, primary ZABs were assembled by D-CFs, N/S-CFs, and Pt/C as cathode catalysts. Polarization and power density curves are generally used to assess the performance of ZABs. D-CFs- and Pt/C-based ZABs both display an open circuit voltage of $\sim 1.33 \text{ V}$ in Fig. 5a. In addition,

D-CFs reveal a peak power density of 238 mW cm^{-2} , while Pt/C is only 154 mW cm^{-2} . Remarkably, compared with other metal-free carbon catalysts, the application of D-CFs in ZABs with high power density still display significant advantages (Fig. 5b and Table S3). Galvanostatic discharge curves of ZABs assembled with D-CFs, N/S-CFs, and Pt/C at a limiting diffusion current density of 10 mA cm^{-2} are revealed in Fig. 5c. After 48 h, D-CFs maintain the discharge voltage of 95.3%, while Pt/C is only 93.5%. At this time, the discharge voltage of D-CFs is 1.17 V, which is 30 mV higher than that of Pt/C (1.14 V). In addition, N/S-CFs can only be discharged continuously for $\sim 42 \text{ h}$ due to the low specific capacity. The rate performance is also assessed via increasing the discharging current densities of 25, 100, 200 and 300 mA cm^{-2} , where D-CFs-based ZABs exhibit potential platform of 1.22, 1.08, 0.93 and 0.78 V, respectively (Fig. 5d). The stable platforms of D-CFs-based ZABs are significantly higher than those of N/S-CFs- and Pt/C-based ZABs. The specific

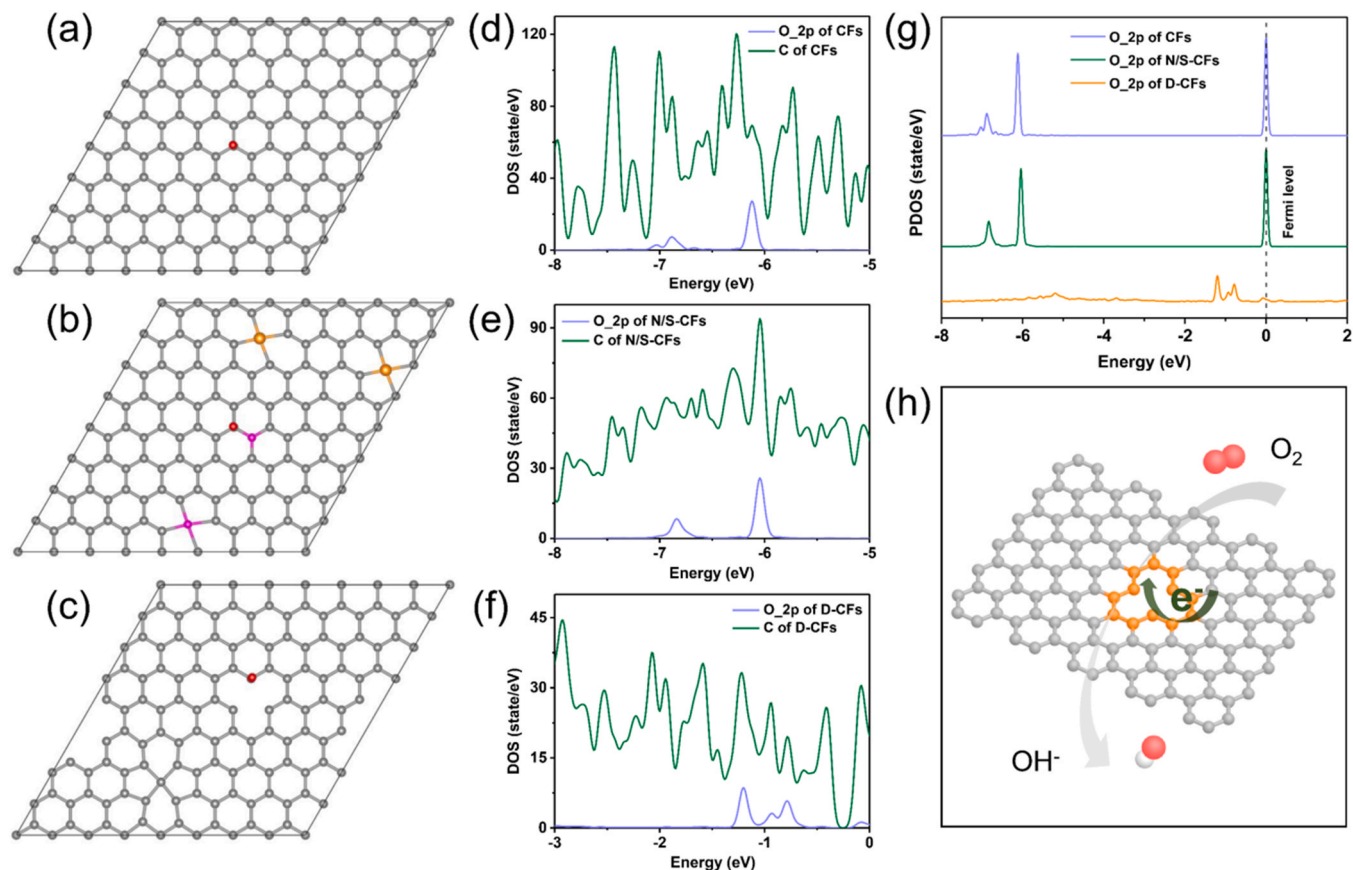


Fig. 6. The top views of optimized structures of (a) CFs, (b) N/S-CFs, and (c) D-CFs. Red balls represent the adsorbed O_2 molecule at active sites (silver: C, purple: N, and yellow: S). The density of states (DOS) of C atoms and the partial density of states (PDOS) of adsorbed O atoms on (d) CFs, (e) N/S-CFs, and (f) D-CFs. (g) PDOS of adsorbed O atoms on CFs, N/S-CFs and D-CFs. (h) The schematic mechanism of D-CFs for ORR.

capacity of D-CFs-based ZABs is up to $795 \text{ mA h g}_{\text{Zn}}^{-1}$, much superior to that of Pt/C-based ZABs ($677 \text{ mA h g}_{\text{Zn}}^{-1}$) through the mass of normalized zinc consumption (Fig. S12). Notably, the air cathode catalyzed by D-CFs maintains a stable discharge platform for 48 h with little voltage loss at a discharge current density of 10 mA cm^{-2} . After each discharge, once the consumed Zn anode and electrolyte are supplemented, the air electrode could work continuously (Fig. 5e). Furthermore, two series ZABs can successfully light the LED with a rated voltage of 2 V (Fig. 5e inset). In a word, after removing the doped N and S atoms, the recombination of carbon atoms changes the electronic structure of the defective carbon atoms, which makes D-CFs obtain outstanding ORR activity. The excellent performance and rich sources, make D-CFs possible to replace Pt-based catalysts and realize large-scale application of ZABs. The oxygen evolution reaction (OER) performance of D-CFs was studied in 1 M KOH via the standard three-electrode system. To achieve 10 mA cm^{-2} current density (a common criterion to assess OER performance), D-CFs requires a potential (vs. RHE) of 1.68 V, which is much higher than that of Ir/C (1.44 V), indicating the poor OER activity of D-CFs [11].

3.4. DFT calculations

DFT calculations were used to study the effect of defect sites on ORR reaction kinetics. Fig. 6a-c display the structures of fully relaxed CFs, N/S-CFs and D-CFs where O_2 molecules are adsorbed on active sites, respectively. When the O_2 molecules are adsorbed on active C atoms, the interaction between C atoms and O atoms makes that the 2p orbital of O atoms are hybridized with the C atoms orbital [50]. The hybridization energy levels between the orbitals of O atom and C atom in CFs are far away from Fermi level, which indicates that O_2 molecule is inert to

adsorption at CFs sites (Fig. 6d). As displayed in Fig. 6e, owing to the optimized electronic environment of adjacent C atoms by doping N/S atoms, the hybridization energy levels of O atom and C atom slightly rise to Fermi level. It makes that N/S-CFs reveal more excellent ORR performance than CFs, but still far away from the performance of Pt-based catalysts. Remarkably, as shown in Fig. 6f, the hybridization energy levels of defective C atom and adsorbed O atom are very close to Fermi level, which indicates that O_2 molecules are more inclined to adsorb on defective C atoms in D-CFs [51]. As shown in Fig. 6g, the 2p orbital of O atoms adsorbed on defective carbon atoms is much closer to Fermi level than that of CFs and N/S-CFs. The energy of 2p orbitals of adsorbed O atom is reduced through the electronic reflux, which is confirmed by the significant decrease of 2p orbital energy of adsorbed O atom on defective C atom [35]. Thus, the adsorption system becomes stable and then D-CFs reveal the comparable activity to Pt/C catalyst. In a word, the electronic environment of C atoms is optimized by the defect sites, which makes that O_2 molecules are more inclined to adsorb on defective C atoms. In addition, the high-density electrons of the defect sites further accelerate the electron transfer in ORR process, which leads to excellent catalytic performance of D-CFs.

4. Conclusion

In summary, we prepared D-CFs as pure carbon ORR electrocatalysts by using calcium alginate with rich sources as the precursors. D-CFs display an initial potential of 0.92 V vs. RHE and a limiting diffusion current density of 5.38 mA cm^{-2} in 0.1 M KOH electrolyte, which is comparable to those of Pt/C catalyst. Particularly, D-CFs reveal excellent performance in primary ZABs application, whose peak power density is 238 mW cm^{-2} while Pt/C is only 154 mW cm^{-2} . It is ascribed to the

formation of intrinsic carbon defect sites in D-CFs via carbon atom recombination after removing doped nitrogen and sulfur atoms. Specifically, the hybridization energy levels of defective C atom and adsorbed O atom of D-CFs are very close to Fermi level. Thus, O₂ molecules are more inclined to adsorb on defective carbon atoms than that of CFs and N/S-CFs, which provide effective catalytic active sites for ORR. Low cost and outstanding ORR catalytic activity make D-CFs become a possible candidate to replace Pt-based catalysts for large-scale application of ZABs.

CRedit authorship contribution statement

Xiaoliang Zhao: Designed the experiments, Wrote the manuscript. **Xuezhen Yu, Chaosheng Bao:** Synthesized the electro-catalysts. **Wenqing Xu, Jingfei Xue:** Characterized structures of materials. **Bin Hui:** Performed electrochemical experiments. **Shuai Chen:** Conducted electron microscopy measurements. **Shishan Xin:** Performed the theoretical calculations. **Jianwei Zhang, Xilin She, Dongjiang Yang:** Revised the manuscript with input from all authors. All authors discussed the results.

Declaration of Competing Interest

The authors declare that they have no known competing financial interests or personal relationships that could have appeared to influence the work reported in this paper.

Acknowledgments

This research is financially supported by the National Natural Science Foundation of China (21501105 and 51808303), the Applied Basic Research of Qingdao City (19-6-2-74-cg), Taishan Scholar Foundation (ts201712030), and Outstanding Youth of Natural Science in Shandong Province (JQ201713), State Key Laboratory of Bio-Fibers and Eco-Textiles (Qingdao University, No. ZKT25 and ZKT30).

Appendix A. Supplementary material

Supporting Information contains this information is available free of charge via the Internet.

Appendix B. Supporting information

Supplementary data associated with this article can be found in the online version at [doi:10.1016/j.apcatb.2021.120785](https://doi.org/10.1016/j.apcatb.2021.120785).

References

- [1] Z. Li, W. Niu, Z. Yang, N. Zaman, W. Samarakoon, M. Wang, A. Kara, M. Lucero, M. V. Vyas, H. Cao, H. Zhou, G.E. Sterbinsky, Z. Feng, Y. Du, Y. Yang, Stabilizing atomic Pt with trapped interstitial F in alloyed PtCo nanosheets for high-performance zinc-air batteries, *Energy Environ. Sci.* 13 (2020) 884–895, <https://doi.org/10.1039/C9EE02657F>.
- [2] K. Wu, L. Zhang, Y. Yuan, L. Zhong, Z. Chen, X. Chi, H. Lu, Z. Chen, R. Zou, T. Li, C. Jiang, Y. Chen, X. Peng, J. Lu, An iron-decorated carbon aerogel for rechargeable flow and flexible Zn-air batteries, *Adv. Mater.* 32 (2020), 2002292, <https://doi.org/10.1002/adma.202002292>.
- [3] X. Duan, S. Ren, N. Pan, M. Zhang, H. Zheng, MOF-derived Fe₂Co@N-C bifunctional oxygen electrocatalysts for Zn-air batteries, *J. Mater. Chem. A* 8 (2020) 9355–9363, <https://doi.org/10.1039/d0ta02825h>.
- [4] F. Yang, J. Xie, D. Rao, X. Liu, J. Jiang, X. Lu, Octahedral distortion enhances exceptional oxygen catalytic activity of calcium manganite for advanced Zn-air batteries, *Nano Energy* 85 (2021), 106020, <https://doi.org/10.1016/j.nanoen.2021.106020>.
- [5] G. Yang, J. Zhu, P. Yuan, Y. Hu, G. Qu, B.A. Lu, X. Xue, H. Yin, W. Cheng, J. Cheng, W. Xu, J. Li, J. Hu, S. Mu, J.N. Zhang, Regulating Fe-spin state by atomically dispersed Mn-N in Fe-N-C catalysts with high oxygen reduction activity, *Nat. Commun.* 12 (2021) 1734, <https://doi.org/10.1038/s41467-021-21919-5>.
- [6] X.F. Lu, Y.J. Fang, D.Y. Luan, X.W. Lou, Metal-organic frameworks derived functional materials for electrochemical energy storage and conversion: a mini review, *Nano Lett.* 21 (2021) 1555–1565, <https://doi.org/10.1021/acs.nanolett.0c04898>.
- [7] Y. Zhang, L. Lu, S. Zhang, Z. Lv, D. Yang, J. Liu, Y. Chen, X. Tian, H. Jin, W. Song, Biomass chitosan derived cobalt/nitrogen doped carbon nanotubes for the electrocatalytic oxygen reduction reaction, *J. Mater. Chem. A* 6 (2018) 5740–5745, <https://doi.org/10.1039/C7TA11258K>.
- [8] Q. Liu, X. Liu, Y. Xie, F. Sun, Z. Liang, L. Wang, H. Fu, N-Doped carbon coating enhances the bifunctional oxygen reaction activity of CoFe nanoparticles for a highly stable Zn-air battery, *J. Mater. Chem. A* 8 (2020) 21189–21198, <https://doi.org/10.1039/D0TA08114K>.
- [9] K. Jiang, S. Back, A.J. Akey, C. Xia, Y. Hu, W. Liang, D. Schaak, E. Stavitski, J. K. Norskov, S. Siahrostami, H. Wang, Highly selective oxygen reduction to hydrogen peroxide on transition metal single atom coordination, *Nat. Commun.* 10 (2019) 3997, <https://doi.org/10.1038/s41467-019-11992-2>.
- [10] X. Huang, T. Shen, T. Zhang, H. Qiu, X. Gu, Z. Ali, Y. Hou, Efficient oxygen reduction catalysts of porous carbon nanostructures decorated with transition metal species, *Adv. Energy Mater.* 10 (2019), 1900375, <https://doi.org/10.1002/aenm.201900375>.
- [11] G.T. Fu, J. Wang, Y.F. Chen, Y. Liu, Y.W. Tang, J.B. Goodenough, J.M. Lee, Exploring indium-based ternary thiospinel as conceivable high-potential air-cathode for rechargeable Zn-air batteries, *Adv. Energy Mater.* 8 (2018), 1802263, <https://doi.org/10.1002/aenm.201802263>.
- [12] I.Y. Kim, S. Kim, S. Premkumar, J.H. Yang, S. Umapathy, A. Vinu, Thermodynamically stable mesoporous C₃N₇ and C₃N₆ with ordered structure and their excellent performance for oxygen reduction reaction, *Small* 16 (2020), 1903572, <https://doi.org/10.1002/sml.201903572>.
- [13] S. Zhao, X. Zhao, Insights into the role of singlet oxygen in the photocatalytic hydrogen peroxide production over polyoxometalates-derived metal oxides incorporated into graphitic carbon nitride framework, *Appl. Catal. B: Environ.* 250 (2019) 408–418, <https://doi.org/10.1016/j.apcatb.2019.02.031>.
- [14] J.Y. Zhao, R. Wang, S. Wang, Y.R. Lv, H. Xu, S.Q. Zang, Metal-organic framework-derived Co₉S₈ embedded in N, O and S-tridoped carbon nanomaterials as an efficient oxygen bifunctional electrocatalyst, *J. Mater. Chem. A* 7 (2019) 7389–7395, <https://doi.org/10.1039/c8ta12116h>.
- [15] W. Peng, Y. Wang, X. Yang, L. Mao, J. Jin, S. Yang, K. Fu, G. Li, Co₉S₈ nanoparticles embedded in multiple doped and electrospun hollow carbon nanofibers as bifunctional oxygen electrocatalysts for rechargeable zinc-air battery, *Appl. Catal. B: Environ.* 268 (2020), 118437, <https://doi.org/10.1016/j.apcatb.2019.118437>.
- [16] X. Long, D. Li, B. Wang, Z. Jiang, W. Xu, B. Wang, D. Yang, Y. Xia, Heterocyclization strategy for construction of linear conjugated polymers: efficient metal-free electrocatalysts for oxygen reduction, *Angew. Chem. Int. Ed.* 58 (2019) 11369–11373, <https://doi.org/10.1002/anie.201905468>.
- [17] B. Wang, W. Song, D. Li, X. Long, Y. Xia, Optimizing the oxygen reduction catalytic activity of a bipyridine-based polymer through tuning the molecular weight, *J. Mater. Chem. A* 9 (2021) 3322–3327, <https://doi.org/10.1039/d0ta11969e>.
- [18] X. Xing, R. Liu, M. Anjass, K. Cao, U. Kaiser, G. Zhang, C. Streib, Bimetallic manganese-vanadium functionalized N,S-doped carbon nanotubes as efficient oxygen evolution and oxygen reduction electrocatalysts, *Appl. Catal. B: Environ.* 277 (2020), 119195, <https://doi.org/10.1016/j.apcatb.2020.119195>.
- [19] J. Gu, S. Magagula, J. Zhao, Z. Chen, Boosting ORR/OER activity of graphdiyne by simple heteroatom doping, *Small Methods* 3 (2019), 1800550, <https://doi.org/10.1002/sml.201800550>.
- [20] D. Li, C. Li, L. Zhang, H. Li, L. Zhu, D. Yang, Q. Fang, S. Qiu, X. Yao, Metal-free thiophene-sulfur covalent organic frameworks: precise and controllable synthesis of catalytic active sites for oxygen reduction, *J. Am. Chem. Soc.* 142 (2020) 8104–8108, <https://doi.org/10.1021/jacs.0c02225>.
- [21] Y. Wang, N. Xu, R. He, L. Peng, D. Cai, J. Qiao, Large-scale defect-engineering tailored tri-doped graphene as a metal-free bifunctional catalyst for superior electrocatalytic oxygen reaction in rechargeable Zn-air battery, *Appl. Catal. B: Environ.* 285 (2021), 119811, <https://doi.org/10.1016/j.apcatb.2020.119811>.
- [22] S. Yuan, L.L. Cui, Z. Dou, X. Ge, X. He, W. Zhang, T. Asefa, Bimetallic sites coordinated on N-doped carbons with efficient and durable catalytic activity for oxygen reduction, *Small* 16 (2020), 2000742, <https://doi.org/10.1002/sml.202000742>.
- [23] Y. Zheng, H. Song, S. Chen, X. Yu, J. Zhu, J. Xu, K.A.I. Zhang, C. Zhang, T. Liu, Metal-free multi-heteroatom-doped carbon bifunctional electrocatalysts derived from a covalent triazine polymer, *Small* 16 (2020), 2004342, <https://doi.org/10.1002/sml.202004342>.
- [24] Y. Chang, J. Chen, J. Jia, X. Hu, H. Yang, M. Jia, Z. Wen, The fluorine-doped and defects engineered carbon nanosheets as advanced electrocatalysts for oxygen electroreduction, *Appl. Catal. B: Environ.* 284 (2021), 119721, <https://doi.org/10.1016/j.apcatb.2020.119721>.
- [25] Y. Wang, L. Tao, Z. Xiao, R. Chen, Z. Jiang, S. Wang, 3D Carbon electrocatalysts in situ constructed by defect-rich nanosheets and polyhedrons from NaCl-sealed zeolitic imidazolate frameworks, *Adv. Funct. Mater.* 28 (2018), <https://doi.org/10.1002/adfm.201705356>.
- [26] L. An, B. Huang, Y. Zhang, R. Wang, N. Zhang, T. Dai, P. Xi, C.H. Yan, Interfacial defect engineering for improved portable Zinc-air batteries with a broad working temperature, *Angew. Chem. Int. Ed.* 58 (2019) 9459–9463, <https://doi.org/10.1002/anie.201903879>.
- [27] J. Li, C. Shu, A. Hu, Z. Ran, M. Li, R. Zheng, J. Long, Tuning oxygen non-stoichiometric surface via defect engineering to promote the catalysis activity of Co₃O₄ in Li-O₂ batteries, *Chem. Eng. J.* 381 (2020), 122678, <https://doi.org/10.1016/j.cej.2019.122678>.

- [28] Y. Jia, L. Zhang, A. Du, G. Gao, J. Chen, X. Yan, C.L. Brown, X. Yao, Defect graphene as a trifunctional catalyst for electrochemical reactions, *Adv. Mater.* 28 (2016) 9532–9538, <https://doi.org/10.1002/adma.201602912>.
- [29] Y. Zhang, L. Tao, C. Xie, D. Wang, Y. Zou, R. Chen, Y. Wang, C. Jia, S. Wang, Defect engineering on electrode materials for rechargeable batteries, *Adv. Mater.* 32 (2020), 1905923, <https://doi.org/10.1002/adma.201905923>.
- [30] H. Lu, L. Zhuang, R.R. Gaddam, X. Sun, C. Xiao, T. Duignan, Z. Zhu, X.S. Zhao, Microcrystalline cellulose-derived porous carbons with defective sites for electrochemical applications, *J. Mater. Chem. A* 7 (2019) 22579–22587, <https://doi.org/10.1039/c9ta05891e>.
- [31] H.J. Qiu, P. Du, K. Hu, J. Gao, H. Li, P. Liu, T. Ina, K. Ohara, Y. Ito, M. Chen, Metal and nonmetal Codoped 3D nanoporous graphene for efficient bifunctional electrocatalysis and rechargeable Zn-air batteries, *Adv. Mater.* 31 (2019), 1900843, <https://doi.org/10.1002/adma.201900843>.
- [32] J. Meng, H. Lei, X. Li, J. Qi, W. Zhang, R. Cao, Attaching cobalt corroles onto carbon nanotubes: verification of four-electron oxygen reduction by mononuclear cobalt complexes with significantly improved efficiency, *ACS Catal.* 9 (2019) 4551–4560, <https://doi.org/10.1021/acscatal.9b00213>.
- [33] Y. Zou, X. Yang, C. Lv, T. Liu, Y. Xia, L. Shang, G.I. Waterhouse, D. Yang, T. Zhang, Multishelled Ni-rich $\text{Li}(\text{Ni}_x\text{Co}_y\text{Mn}_z)\text{O}_2$ hollow fibers with low cation mixing as high-performance cathode materials for Li-ion batteries, *Adv. Sci.* 4 (2017), 1600262, <https://doi.org/10.1002/adv.201600262>.
- [34] P. Li, Z. Jin, Y. Qian, Z. Fang, D. Xiao, G. Yu, Supramolecular confinement of single Cu atoms in hydrogel frameworks for oxygen reduction electrocatalysis with high atom utilization, *Mater. Today* 35 (2020) 78–86, <https://doi.org/10.1016/j.mattod.2019.10.006>.
- [35] C. Wei, Y. Sun, G.G. Scherer, A.C. Fisher, M. Sherburne, J.W. Ager, Z.J. Xu, Surface composition dependent ligand effect in tuning the activity of Nickel-Copper bimetallic electrocatalysts toward hydrogen evolution in Alkaline, *J. Am. Chem. Soc.* 142 (2020) 7765–7775, <https://doi.org/10.1021/jacs.9b12005>.
- [36] Q. Song, J. Li, S. Wang, J. Liu, X. Liu, L. Pang, H. Li, H. Liu, Enhanced electrocatalytic performance through body enrichment of Co-based bimetallic nanoparticles in situ embedded porous N-doped carbon spheres, *Small* 15 (2019), 1903395, <https://doi.org/10.1002/sml.201903395>.
- [37] Y. Mun, S. Lee, K. Kim, S. Kim, S. Lee, J.W. Han, J. Lee, Versatile strategy for tuning ORR activity of a single Fe-N4 site by controlling electron-withdrawing/donating properties of a carbon plane, *J. Am. Chem. Soc.* 141 (2019) 6254–6262, <https://doi.org/10.1021/jacs.8b13543>.
- [38] X. Xiao, X. Li, Z. Wang, G. Yan, H. Guo, Q. Hu, L. Li, Y. Liu, J. Wang, Robust template-activator cooperated pyrolysis enabling hierarchically porous honeycombed defective carbon as highly-efficient metal-free bifunctional electrocatalyst for Zn-air batteries, *Appl. Catal. B: Environ.* 265 (2020), 118603, <https://doi.org/10.1016/j.apcatb.2020.118603>.
- [39] B.M. Matsagar, R.X. Yang, S. Dutta, Y.S. Ok, K.C.W. Wu, Recent progress in the development of biomass-derived nitrogen-doped porous carbon, *J. Mater. Chem. A* 9 (2021) 3703–3728, <https://doi.org/10.1039/d0ta09706c>.
- [40] G. Tao, L. Zhang, L. Chen, X. Cui, Z. Hua, M. Wang, J. Wang, Y. Chen, J. Shi, N-doped hierarchically macro/mesoporous carbon with excellent electrocatalytic activity and durability for oxygen reduction reaction, *Carbon* 86 (2015) 108–117, <https://doi.org/10.1016/j.carbon.2014.12.102>.
- [41] X. Yu, S. Lai, S. Xin, S. Chen, X. Zhang, X. She, T. Zhan, X. Zhao, D. Yang, Coupling of iron phthalocyanine at carbon defect site via π - π stacking for enhanced oxygen reduction reaction, *Appl. Catal. B: Environ.* 280 (2021), 119437, <https://doi.org/10.1016/j.apcatb.2020.119437>.
- [42] W. Wan, X. Liu, H. Li, X. Peng, D. Xi, J. Luo, 3D carbon framework-supported CoNi nanoparticles as bifunctional oxygen electrocatalyst for rechargeable Zn-air batteries, *Appl. Catal. B: Environ.* 240 (2019) 193–200, <https://doi.org/10.1016/j.apcatb.2018.08.081>.
- [43] Z. Li, H. He, H. Cao, S. Sun, W. Diao, D. Gao, P. Lu, S. Zhang, Z. Guo, M. Li, R. Liu, D. Ren, C. Liu, Y. Zhang, Z. Yang, J. Jiang, G. Zhang, Atomic Co/Ni dual sites and Co/Ni alloy nanoparticles in N-doped porous Janus-like carbon frameworks for bifunctional oxygen electrocatalysis, *Appl. Catal. B: Environ.* 240 (2019) 112–121, <https://doi.org/10.1016/j.apcatb.2018.08.074>.
- [44] Y. Zhu, X. Liu, S. Jin, H. Chen, W. Lee, M. Liu, Y. Chen, Anionic defect engineering of transition metal oxides for oxygen reduction and evolution reactions, *J. Mater. Chem. A* 7 (2019) 5875–5897, <https://doi.org/10.1039/c8ta12477a>.
- [45] Y. Chen, F. Su, H. Xie, R. Wang, C. Ding, J. Huang, Y. Xu, L. Ye, One-step construction of S-scheme heterojunctions of N-doped MoS_2 and S-doped $\text{g-C}_3\text{N}_4$ for enhanced photocatalytic hydrogen evolution, *Chem. Eng. J.* 404 (2021), 126498, <https://doi.org/10.1016/j.cej.2020.126498>.
- [46] D.H. Li, Y. Jia, G.J. Chang, J. Ren, H.W. Liu, J.C. Wang, Y.F. Hu, Y.Z. Xia, D. J. Yang, X.D. Yao, A defect-driven metal-free electrocatalyst for oxygen reduction in acidic electrolyte, *Chem* 4 (2018) 2345–2356, <https://doi.org/10.1016/j.chempr.2018.07.005>.
- [47] K.G. Qu, Y. Zheng, Y. Jiao, X.X. Zhang, S. Dai, S.Z. Qiao, Polydopamine-inspired, dual heteroatom-doped carbon nanotubes for highly efficient overall water splitting, *Adv. Energy Mater.* 7 (2017), 1602068, <https://doi.org/10.1002/aenm.201602068>.
- [48] F. Xiao, X. Yang, H. Wang, J. Xu, Y. Liu, D.Y.W. Yu, A.L. Rogach, Covalent encapsulation of sulfur in a MOF-derived S, N-doped porous carbon host realized via the vapor-infiltration method results in enhanced sodium-sulfur battery performance, *Adv. Energy Mater.* 10 (2020), 2000931, <https://doi.org/10.1002/aenm.202000931>.
- [49] Y. Xiong, Y. Yang, F.J. DiSalvo, H.D. Abruna, Metal-organic framework-derived Co-Fe bimetallic oxygen reduction electrocatalysts for alkaline fuel cells, *J. Am. Chem. Soc.* 141 (2019) 10744–10750, <https://doi.org/10.1021/jacs.9b03561>.
- [50] Z.W. Chen, X.Y. Lang, Q. Jiang, Discovery of cobweb-like MoC_6 and its application for nitrogen fixation, *J. Mater. Chem. A* 6 (2018) 9623–9628, <https://doi.org/10.1039/C8TA03481H>.
- [51] Z. Chen, J. Zhao, C.R. Cabrera, Z. Chen, Computational screening of efficient single-atom catalysts based on graphitic carbon nitride ($\text{g-C}_3\text{N}_4$) for nitrogen electroreduction, *Small Methods* 3 (2018), 1800368, <https://doi.org/10.1002/smt.201800368>.